

Structure and Electronic Properties of SrTiO₃–TiO₂ Eutectic for Water Splitting Applications

Yefei Guo, Hafiz Muhammad Zeeshan, Mouhui Yan, Weimin Qin, Wanting Yang, Shixun Cao, Yuriy Dedkov,* and Elena Voloshina*

Semiconductors with bandgaps and edges corresponding to the solar energy spectrum are found to be suitable for the water splitting applications using photoelectrochemical reactions. However, many present-day materials used in these applications do not have high stability and/or high effectiveness over the complete sunlight spectral range. The recently proposed eutectic compounds, which combine two or more semiconducting materials, can overcome many present difficulties and extend the light absorbance spectrum improving the effectiveness of the water splitting cells. Herein, structural and electronic properties studies of the SrTiO₃–TiO₂ eutectic material, which is a representative example of this family, are presented. It is found that structural properties of this material, particularly the phase separation and formation of the sharp interface between two phases, can be significantly improved up on the thermal annealing, which is very important for their application in the water splitting reactors. The findings present the deep understanding of the interface structure and electronic properties of the SrTiO₃–TiO₂ eutectic, which can help to improve the functionality of these class of materials in different applications.

reactions using sunlight. In photocatalytic water splitting, the energy of solar radiation is used directly to dissociate water molecules into hydrogen and oxygen. In such approach, an electron–hole pair is produced upon the illumination and then the excited electrons are used to reduce the acceptor (H⁺), whereas the holes are used for the oxidation of the donor molecule (OH[−]).

The mechanism of water splitting in the presence of semiconductors was discussed in many publications:^[1,3–5] two half reactions—reduction and oxidation processes—are observed at the surface of semiconductor requiring a minimum energy of 1.23 eV for water splitting. Therefore, materials with a bandgap greater than this value are needed for the effective water splitting and hydrogen production. TiO₂ with the bandgap of $E_g \approx 3.0$ eV is the most commonly used photocatalyst since Fujishima


and Honda found that TiO₂ can be used as an anode in the photoelectrochemical system for H₂ production in water splitting reaction.^[6,7] After this discovery many materials, like metal oxides (e.g., ZnO, $E_g \approx 3.3$ eV; SrTiO₃, $E_g \approx 3.2$ eV; Fe₂O₃, $E_g \approx 2.1$ eV), nitrides (e.g., Ta₃N₅, $E_g \approx 2.1$ eV; GaN, $E_g \approx 3.4$ eV), and chalcogenides (e.g., GdSe, CdS, GeSe, $E_g \approx 1.5 - 3.5$ eV), were tested for the efficient water splitting applications^[3,8,9] and it was also found that many factors, like

1. Introduction

The present-day demands for the green energy production using hydrogen gas, which is generated via the water splitting reaction, require the search for more efficient, low-cost, and robust materials and systems which can be used in these processes.^[1–3] One of the promising approaches for production of hydrogen from water is the utilization of semiconductors in photocatalytic

Y. Guo, M. Yan, Y. Dedkov, E. Voloshina
Department of Physics
Shanghai University
99 Shangda Road, 200444 Shanghai, P. R. China
E-mail: dedkov@shu.edu.cn; voloshina@shu.edu.cn

H. M. Zeeshan
Institute of Chemical Reaction Engineering
Hamburg University of Technology (TUHH)
Eißendorfer Straße 38, 21073 Hamburg, Germany

 The ORCID identification number(s) for the author(s) of this article can be found under <https://doi.org/10.1002/aesr.202300136>.

© 2023 The Authors. Advanced Energy and Sustainability Research published by Wiley-VCH GmbH. This is an open access article under the terms of the Creative Commons Attribution License, which permits use, distribution and reproduction in any medium, provided the original work is properly cited.

DOI: 10.1002/aesr.202300136

W. Qin
State Key Laboratory of Advanced Special Steels & Shanghai Key Laboratory of Advanced Ferrometallurgy
School of Materials Science and Engineering
Shanghai University
99 Shangda Road, 200444 Shanghai, P. R. China

W. Yang, S. Cao
Department of Physics
Materials Genome Institute and International Center for Quantum and Molecular Structures
99 Shangda Road, 200444 Shanghai, P. R. China

E. Voloshina
Institute of Chemistry and Biochemistry
Freie Universität Berlin
Arnimallee 22, 14195 Berlin, Germany

solution pH, temperature, light intensity, materials' bandgaps, etc., can play a crucial role in the efficiency of photoelectrochemical devices.

Different ways were proposed in order to modify the properties of photoanodes. The natural way here is the doping of semi-conducting materials with ions of different elements in order to

extend the light absorption spectrum, increase the electron-hole pair creation efficiency, and change mobilities of the carriers. For example, in the particular case of TiO_2 , the carbon quantum dots at the surface lead to the enhancement of the electron transfer at the interface with the respective reduction of impedance.^[10] In case of the sol-gel method used to synthesize Ce-doped TiO_2

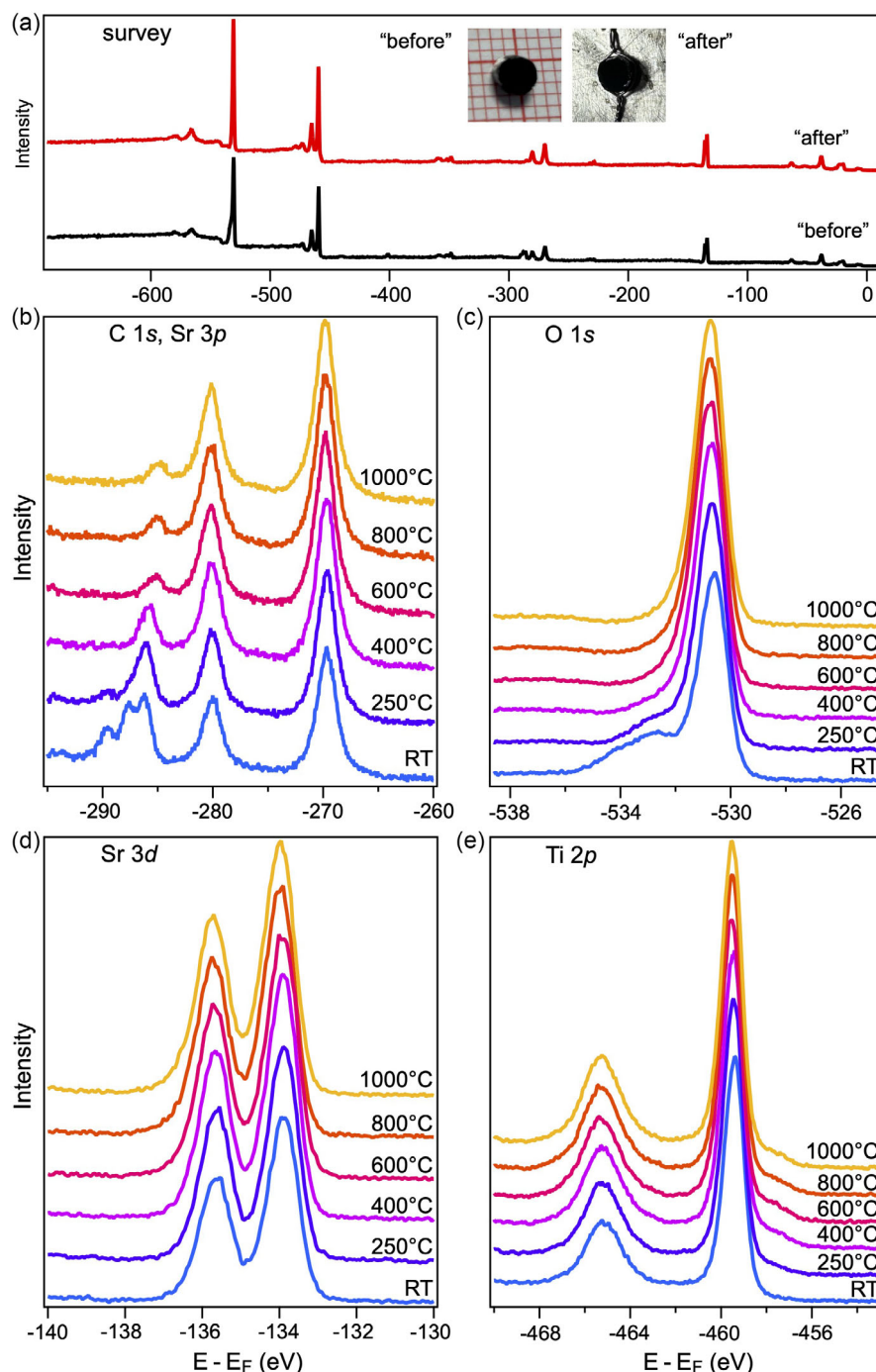


Figure 1. a) Survey XPS spectra collected “before” and “after” annealing of $\text{SrTiO}_3\text{-TiO}_2$ eutectic at 1000°C . Inset shows the photographs of the $\text{SrTiO}_3\text{-TiO}_2$ sample “before” and “after” thermal annealing (later photo was made for the sample mounted on the Mo sample-holder). High-resolution XPS spectra of $\text{SrTiO}_3\text{-TiO}_2$ collected during stepwise annealing: b) C 1s and Sr 3p, c) O 1s, d) Sr 3d, and e) Ti 2p. Annealing temperatures are marked for every spectrum.

nanocomposites, the formation of impurity-induced energy levels, which extend the absorption spectrum, was found.^[11] Also, as was theoretically demonstrated, iodine can be considered as the best dopant due to its incorporation at Ti sites in the TiO₂ matrix, whereas nitrogen is considered as the minimum efficient dopant due to its p-type nature.^[12–14] The discovery of “black” TiO₂ with a bandgap of only 1.5 eV and increased photocatalytic activity indicated the importance of the used synthesis methods on the tuning of the doping level and morphology of this material.^[15,16]

One of the promising ways to increase the efficiency of semiconducting materials in water splitting applications is the recently proposed approach to use them in the so-called eutectic composites (compounds) and to utilize the μ -pulling method for their synthesis (for recent overview, see ref. [3]). In such a way (μ -pulling method) produced, e.g., binary eutectic compounds consist of two crystalline phases combining electronic, optical and photoelectrochemical properties of both, thus increasing the absorption spectrum for sunlight. One of the representative examples of eutectic compounds is the SrTiO₃–TiO₂ (STO–TO) combination, which demonstrated the light absorption over a wide spectral range and efficient charge-carriers separation.^[17–19] This semiconductor composite was used for the fabrication of stable photoanode and yielded in the experiments photocurrents up to 8.5 mA cm⁻² at 1.5 V versus a normal hydrogen electrode (NHE) after 30 h of stability testing under 600 mW cm⁻² of solar irradiation, demonstrating its very high potential for the water splitting applications. In such composite materials, a sharp and clear interface between two phases can improve the electrical contact between them, which is important for the charge-carriers separation.^[20] Additionally, the natural

oxygen defects in eutectic compound (SrTiO_{3-x}–TiO_{2-x}) caused by the synthesis process can also improve the photocatalytic efficiency.^[21,22] However, the detailed studies of the crystallographic structure and electronic properties of bulk eutectic compounds and interfaces between phases, particularly for the SrTiO₃–TiO₂ eutectic compound, are not presented in the literature.

Here, we present first detailed spectroscopic and microscopic studies of the electronic and crystallographic structure of the semiconducting SrTiO₃–TiO₂ eutectic compound. Using X-ray photoelectron spectroscopy (XPS), scanning electron microscopy (SEM), and high-resolution transmission electron microscopy (HR-TEM) methods combined with energy-dispersive X-ray (EDX) analysis, we trace the morphological and structural changes in this compound upon thermal annealing in vacuum conditions. Our spectroscopic studies clearly indicate the increased number of oxygen defects upon annealing. At the same time, the microscopic results demonstrate the improved crystallographic order of bulk and interface between two materials after thermal treatment. Using the HR-TEM data for the SrTiO₃–TiO₂ compound, we build a crystallographic model for the interface between two phases, which surprisingly indicate the parallel arrangement of two close-packed planes, SrTiO₃(111) and TiO₂(110). As found, the calculated electronic properties of the obtained SrTiO₃–TiO₂ structures are a combination of the respective contributions of both phases. Our results clearly point to the importance of the postsynthesis thermal treatment of the semiconducting eutectic compounds that can significantly improve the photocatalytic properties of these systems. The current understanding of the structural and electronic properties of these compounds will help to improve them for further desired applications in different areas.

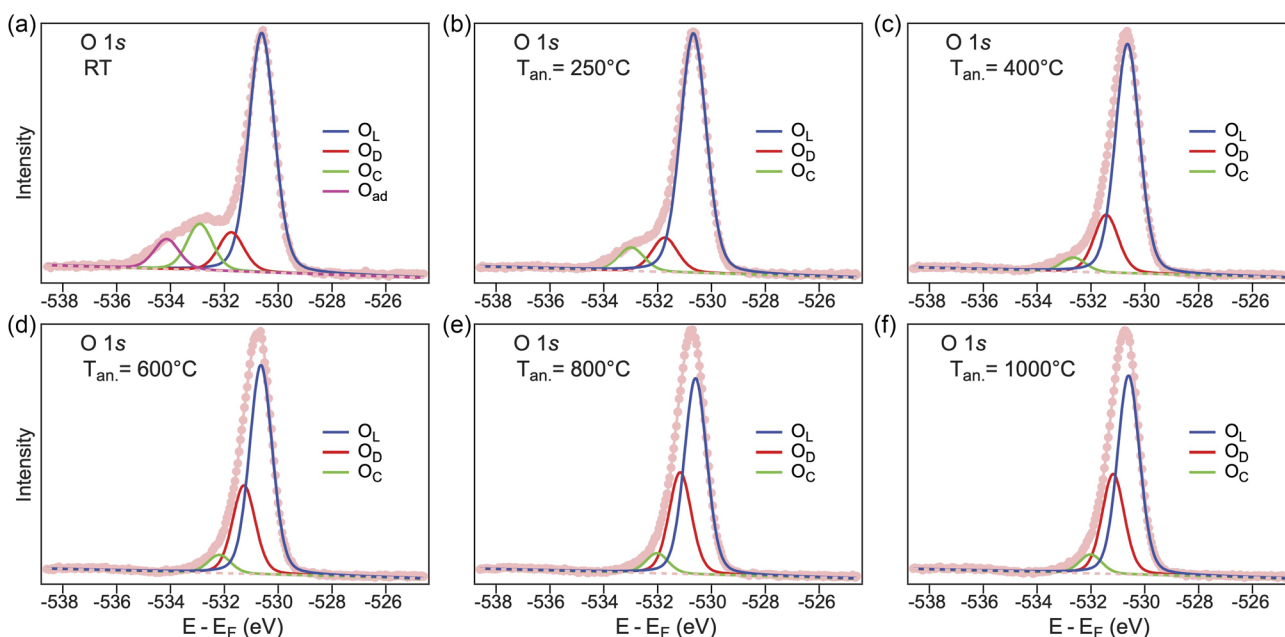


Figure 2. Results of fit procedure for O 1s XPS spectra collected after respective thermal annealing steps: a) RT, b) 250 °C, c) 400 °C, d) 600 °C, e) 800 °C, and f) 1000 °C, respectively. O_L, O_D, O_C, and O_{ad} correspond to oxygen atoms in the SrTiO₃–TiO₂ lattices, connected with oxygen vacancies, assigned to C–O bond in the SrTiO₃–TiO₂ bulk, and OH-adsorbates.

2. Results and Discussion

The as-grown and as-cut polished and freshly cleaned STO–TO sample has a black color (see inset of **Figure 1a**), indicating the large deficiency of oxygen in the sample as confirmed by our experiments (see below). In the present work, these samples were stepwise annealed in ultrahigh vacuum (UHV) conditions and the results of XPS studies of STO–TO are summarized in **Figure 1**. Survey spectra measured before thermal treatment (“before”) and after final annealing at 1000 °C (“after”) are presented in **Figure 1a**, indicating the presence of all elements and the total evolution of the spectral shape during treatment. Before thermal annealing, the clear C 1s signal can be identified in the XPS spectra at $E - E_F < -284$ eV (**Figure 1b**, RT = “before”). Three peaks at -286.2 , -287.6 , and -289.5 eV in this spectrum can be assigned to C–O bonds in bulk of the sample as well as to adsorbed CO and CO₂, respectively. At the same time, the “before” O 1s XPS spectrum shows the clear presence of the emission which can be associated with the respective surface contaminations. Our accurate fit of this spectrum presented in **Figure 2a** indicates the presence of two emission lines which can be associated with C–O bonds in the bulk (O_C, $E - E_F \approx -532.9$ eV) and O–H bonds from adsorbed water (O_{ad}, $E - E_F \approx -534.14$ eV). The XPS emissions in this case (“before”) from Sr 3p, Sr 3d, Ti 2p levels show the respective

Table 1. Atomic concentrations as extracted from SEM/EDX and TEM/EDX data for the STO–TO sample “before” and “after” thermal annealing.

–	SEM/EDX		TEM/EDX	
	“Before”	“After”	“Before”	“After”
SrTiO ₃				
Sr	38.1	37.4	30.80	31.62
Ti	39.3	45.5	30.42	35.45
O	22.6	17.1	38.78	32.93
TiO ₂				
Sr	5.5	4.4	0.15	0.20
Ti	60.5	66.7	46.01	46.05
O	34.0	28.9	53.84	53.75

spin–orbit split doublets without any additional satellites (**Figure 1b,d,e**).

The initial thermal annealing of the STO–TO samples at 250 °C for 60 min leads to the fast desorption of surface contaminations as demonstrated by the absence of the respective signals (CO, CO₂, and OH) in the C 1s and O 1s XPS spectra measured after annealing step. Further annealing of STO–TO to 400 °C and above causes the strong reduction of the respective C 1s and O 1s

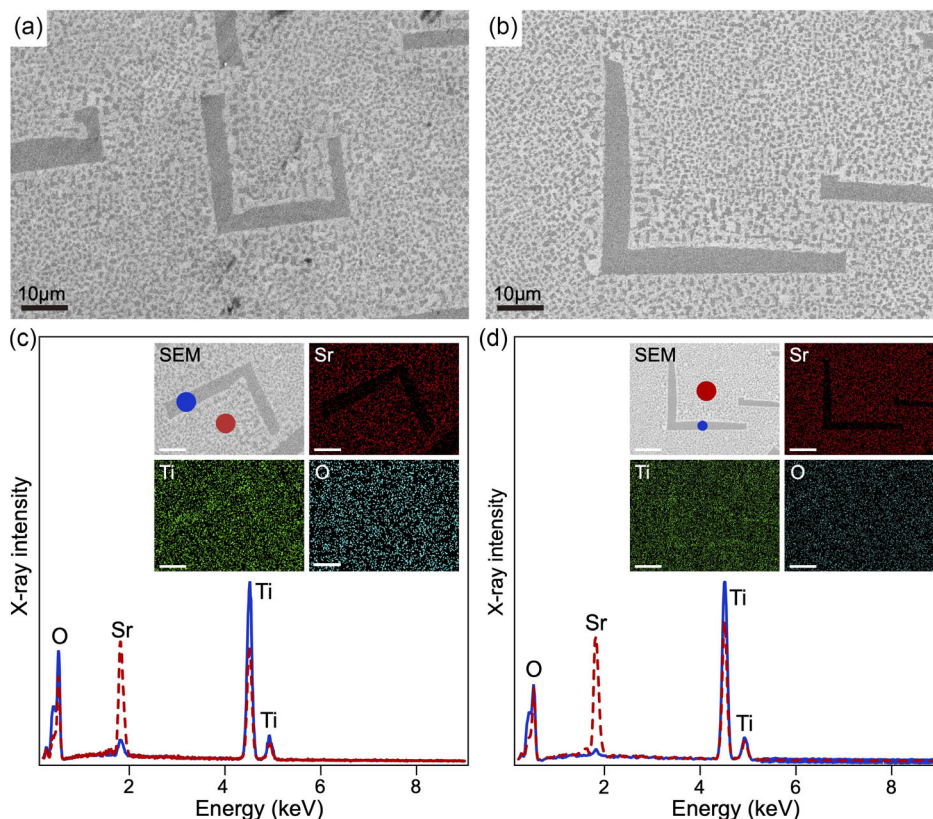


Figure 3. a,b) SEM images of SrTiO₃–TiO₂ collected “before” and “after” annealing of eutectic sample at 1000 °C, respectively. c,d) SEM/EDX plots, collected at the places marked in SEM images (insets) by the corresponding colored circles, “before” and “after” annealing of eutectic sample at 1000 °C, respectively. Insets in both panels show SEM and corresponding elemental EDX maps.

XPS emissions connected with the C–O bonds in the bulk ($E - E_F \approx -286.2$ eV and O_C at $E - E_F \approx -532.9$ eV) that can be connected with the degassing steps of STO–TO bulk. After the stepwise annealing procedure (annealing temperature of 1000 °C, “after”), the STO–TO sample was investigated using SEM and TEM methods combined with EDX analysis (see below).

The presented O 1s and Ti 2p XPS spectra of STO–TO obtained during UHV annealing (Figure 1c,e and 2) indicate the respective increase of the oxygen deficiency in these samples. According to the already mentioned results of the fit routine for the O 1s XPS spectrum measured “before” annealing (Figure 2a), it consists of several emission lines which can be assigned to oxygen atoms in bulk lattices of STO–TO (O_L at $E - E_F \approx -530.6$ eV), near oxygen vacancies (O_D at $E - E_F \approx -531.75$ eV), to C–O bonds in bulk of STO–TO (O_C at $E - E_F \approx -532.9$ eV), and to OH contamination layer (O_{ad} , $E - E_F \approx -534.14$ eV). The O_D fit component corresponds to the dangling bonds of the TiO_{6-x} octahedra associated with oxygen vacancies, including O^- , O_2^- , and O_{2-} .^[23–25] Thermal annealing leads to the absence of the O_{ad} signal in the spectra and to the strong reduction of the O_C emission. At the same time, such annealing to high temperature leads to the significant increase of the number of oxygen vacancies in the STO–TO sample. The relative increase of the number of vacancies can be estimated from the ratio of the XPS fit components corresponding to emission from lattice oxygen atoms and atoms associated with oxygen vacancies, $I(O_L)/I(O_D)$. This value is changed from 6.1 (“before”) to 1.9 (“after”) for the presented data (Figure 2). The effect of increase of the number of oxygen vacancies at the surface region of STO–TO and the respective partial reduction from Ti^{4+} to Ti^{3+} in both $SrTiO_3$ and TiO_2 parts^[26–29] is also visible in the Ti 2p spectrum via appearance of the low binding energy shoulder at $E - E_F \approx -457.7$ eV.

Figure 3 shows the results of combined SEM/EDX studies of STO–TO (a,c) “before” and (b,d) “after” UHV annealing procedure. The respective atomic concentrations of elements in the studied samples are summarized in Table 1. The presented SEM images are in agreement with previously published results,^[17,18] demonstrating the clear separation of two materials which have tetragonal (TiO_2) and cubic ($SrTiO_3$) space groups, respectively. The dark part in SEM images corresponds to TiO_2 as confirmed by the SEM/EDX mapping (Figure 3c,d). Our SEM/EDX data clearly indicate the strong deficiency of oxygen in the prepared STO–TO samples, which explains the black color of the synthesized samples, present and in the previous studies^[17,18] as well as the observation of “black” TiO_2 .^[15,16] From the presented data it is obvious that the overall structure of the STO–TO samples remains the same upon the thermal annealing up to 1000 °C—the same materials phase separation is observed. At the same time, EDX analysis shows the reduction of the oxygen concentration by $\approx 5\%$ for both components of STO–TO compared to the sample “before” annealing. Taking into account the different probing depth of XPS and SEM/EDX, however, we can conclude on the oxygen desorption and surface reduction of STO–TO upon thermal annealing in UHV conditions.

The black color of the STO–TO sample is also confirmed by the UV–vis measurements (Figure 4), which reveal the onset of

optical absorption at ≈ 1.75 eV. This value is much smaller of the bandgaps for reference $SrTiO_3$ and TiO_2 samples, 3.17 and 2.92 eV, respectively. An abrupt change in absorbance spectra observed for both samples, “before” and “after” thermally annealed STO–TO, suggests that the optical gap of the black STO–TO sample is substantially narrowed by intraband transitions. The thermal annealing of the STO–TO sample leads to the increase of the absorbance intensity at ≈ 1.75 eV, which can be assigned to the increase of the oxygen deficiency as was found in the XPS and SEM/EDX experiments. The thermal annealing of the STO–TO sample is accompanied by two competing processes—structural ordering of the STO–TO lattice (as found in HR-TEM measurements; see below) and increase of the oxygen deficiency (according to XPS, SEM/EDX, and HR-TEM/EDX results). The former process leads to the slight increase of the bandgap, whereas the loss of oxygen leads to the decrease of the gap. Therefore, a slight decrease of the bandgaps associated with $SrTiO_3$ and TiO_2 lattices can be a result of these competitive processes, where the increase of the oxygen deficiency prevails (as also confirmed by the increase of the

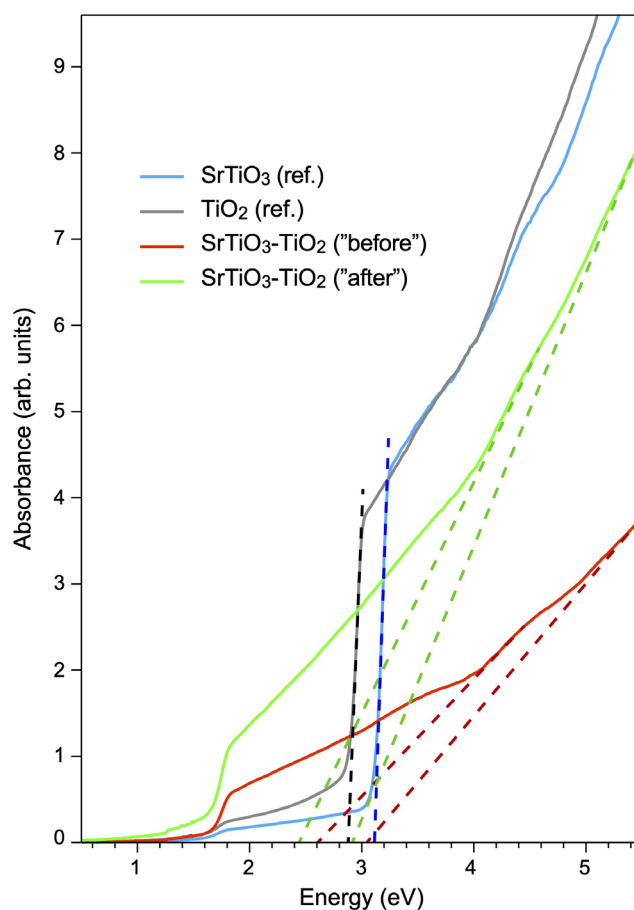


Figure 4. Spectral absorbance of the black $SrTiO_3$ – TiO_2 eutectic samples measured “before” and “after” UHV annealing. The respective reference spectra for the bulk $SrTiO_3$ and TiO_2 samples are presented. The absorbance offset for the reference samples is caused by noncompensated oxygen vacancies. Dotted lines are fits for the respective absorption edges of $SrTiO_3$ and TiO_2 .

absorbance edge at lower energy). It is interesting to note that there is no time-dependent color change for the studied samples indicating their high crystallographic and electronic stability over long time.

The characterization of bulk structure and composition of STO–TO was performed using X-ray diffraction (XRD) and TEM/EDX “before” and “after” UHV thermal annealing (Figure 5). For the as-grown samples “before” annealing, the XRD plots of STO–TO show diffraction peaks which can be assigned to the (100) and (200) diffraction spots of the cubic SrTiO₃ (*Pm* $\bar{3}$ *m* space group) and (002) diffraction spot of rutile TiO₂ (*P4*₂/*mmn* space group) structures, respectively^[18] (Figure 5a). According to XRD, thermal annealing of STO–TO does not lead to the structural changes of the sample confirming the good stability of the prepared samples. At the same time, there is a notable shift of diffraction peaks by $\approx 0.6^\circ$ toward higher diffraction angles for both components, corresponding to the slight reduction of the lattice constants of SrTiO₃ phase from $a = 3.894 \text{ \AA}$ to $a = 3.842 \text{ \AA}$ and TiO₂ phase from $c = 2.948 \text{ \AA}$ to $c = 2.923 \text{ \AA}$, which can be due to the small relaxation of the crystal lattices after annealing. Also, the full width at half maximum (fwhm) values are reduced from 0.24° to 0.22° for

SrTiO₃–(200) and from 0.10° to 0.08° for TiO₂–(001) diffraction peaks, indicating the higher crystallographic order of STO–TO “after” annealing.

The significant improvement of the crystallographic order of STO–TO after thermal annealing is confirmed by high-resolution TEM results (cf., Figure 5b,c). As can be seen, the STO–TO eutectic compound before annealing is characterized by less ordered structure compared to the one measured after thermal annealing. It is reflected in the respective fast Fourier transformation (FFT) images, where increased image background and circles are found in “before” data (Figure 5b). At the same time, the interface between two phases, SrTiO₃ and TiO₂, is not very obvious and extended over several nms, combining structures from two components of the compound. For the “annealed” TEM data, the clear and sharp interface between two phases is resolved with close packed planes of both phases parallel to each other —SrTiO₃(111) || TiO₂(110), which allows to build its model (see below). This observation demonstrates that UHV annealing at 1000 °C reduces the internal stress of the lattices for both parts and make the lattice planes more ordered, improving the crystallization. As was discussed before, the high crystallinity of the two phases in STO–TO and the sharp interface between two phases

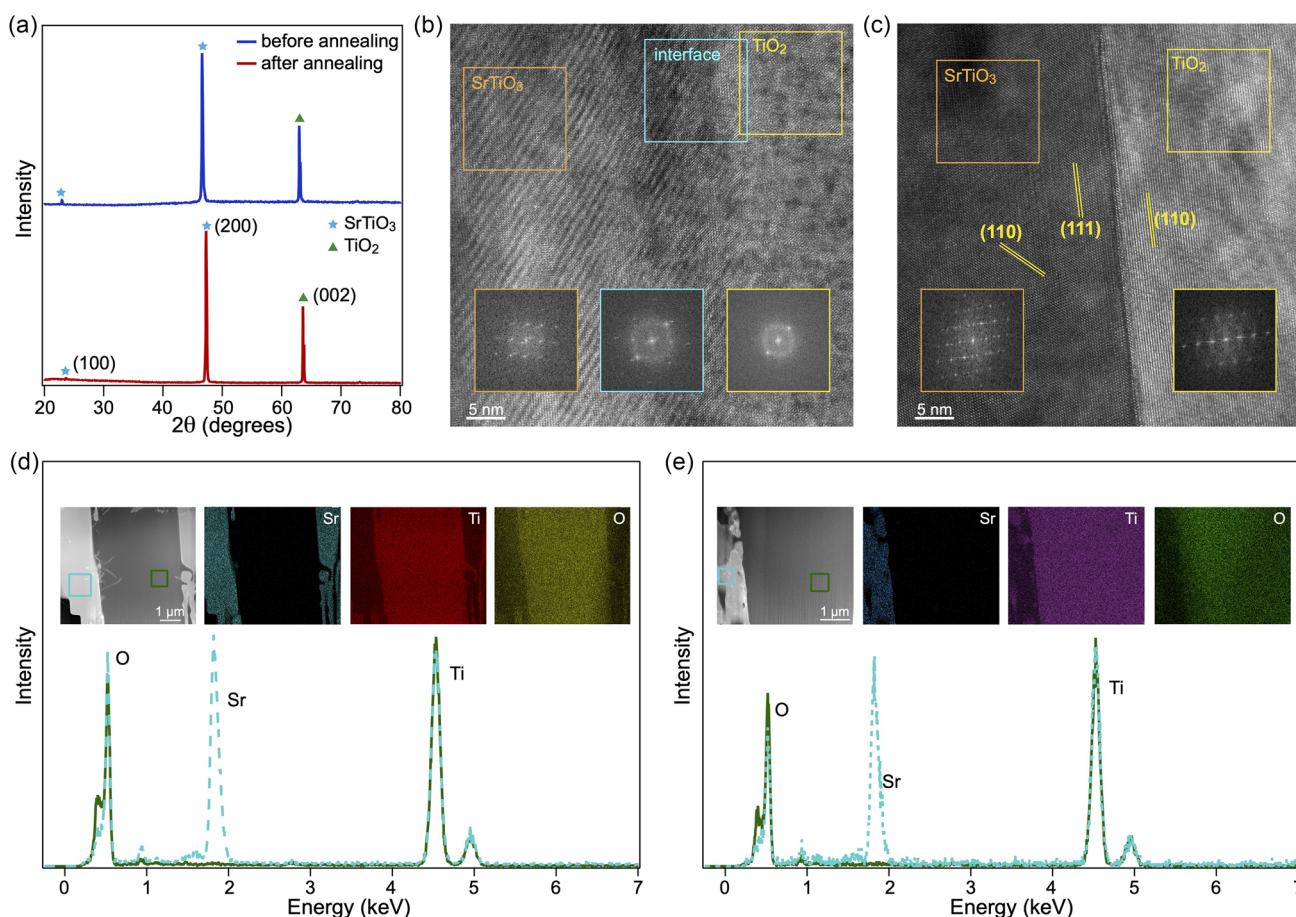


Figure 5. a) XRD plots of SrTiO₃–TiO₂ collected “before” and “after” annealing of eutectic sample at 1000 °C, respectively. b,c) High-resolution TEM images of the interfaces region between SrTiO₃ (left) and TiO₂ phases and collected “before” and “after” annealing of eutectic sample at 1000 °C, respectively. d,e) TEM/EDX plots, collected at the places marked in TEM images (insets) by the corresponding colored rectangles, “before” and “after” annealing of eutectic sample at 1000 °C, respectively. Insets in both panels show TEM and corresponding elemental EDX maps.

can improve electrical contact between them and enhance the charge carriers' mobilities. Such effect is beneficial for the application of these thermally treated STO–TO compounds in energy-related applications such as photoelectric devices, solid oxide fuel cells, etc.^[3,30] As can be also seen, the combined TEM/EDX data (Figure 5d,e and Table 1) also confirm the high deficiency of oxygen in the bulk of STO–TO compound. At the same time, the thermal annealing of STO–TO leads to the increase of the oxygen deficiency only for the SrTiO₃ part by ≈ 6% leaving the oxygen level almost the same for the TiO₂ phase. This indicates that the observed changes in the Ti 2*p* XPS spectra (Figure 1e) are mainly connected with the SrTiO₃ fragments on the surface of STO–TO.

To obtain detailed atomistic insight into the electronic properties of the SrTiO₃–TiO₂ eutectic, we accomplished a density functional theory (DFT) study using the PBE + *U* approach. We first discuss the structural and electronic properties of bulk TiO₂ and SrTiO₃. It is known that titanium dioxide crystallizes in three major different structures, namely, rutile (tetragonal, *P4*₂/*mnm*), brookite (rhombohedral, *Pbca*), and anatase (tetragonal, *I4*₁/*amd*). Following the experimental observations, in this work we focus on the rutile structure, in which unit cell is shown in **Figure 6a**. The basic building block consists of a titanium atom surrounded by six oxygen atoms in a distorted octahedral configuration. Bulk SrTiO₃ crystallizes in a cubic

perovskite structure (*Pm* $\bar{3}m$), in which unit cell is shown in **Figure 6b**. In this structure, the Ti⁴⁺ ions are also sixfold coordinated by O²⁻ ions, whereas each of the Sr²⁺ ions is surrounded by four TiO₆ octahedra. The optimized lattice parameters ($a_{\text{TiO}_2}^{\text{bulk}} = 4.68 \text{ \AA}$, $c_{\text{TiO}_2}^{\text{bulk}} = 3.03 \text{ \AA}$, and $a_{\text{SrTiO}_3}^{\text{bulk}} = 3.97 \text{ \AA}$) are in reasonably good agreement with the respective experimental data known for TiO₂ ($a = 4.58 \text{ \AA}$, $c = 2.95 \text{ \AA}$)^[26] and SrTiO₃ ($a = 3.905 \text{ \AA}$).^[31]

Following the similarity of structural motifs, the electronic structure of the studied materials is also rather similar. Both materials are semiconductors with a bandgap of $E_g = 2.3 \text{ eV}$ [hybrid functional (HSE06) gives $E_g = 3.1 \text{ eV}$ (see **Figure S1**, Supporting Information)]. In both cases, the valence band mainly consists of O 2*p* states, and Ti 3*d* states are major composition for the conduction band. It is known that TiO₂ is easily reduced^[26] and the observed black color of the studied eutectic is due to a large number of oxygen vacancies, as confirmed by the earlier presented EDX results. Following the experimental observations, we have investigated two bulk systems under study after removing 25% of oxygen atoms. These intrinsic defects result in formation of multiple defect states and significant reduction of a bandgap up to 0.76 and 1.51 eV in the case of TiO₂ and SrTiO₃, respectively (**Figure 6c,d**).

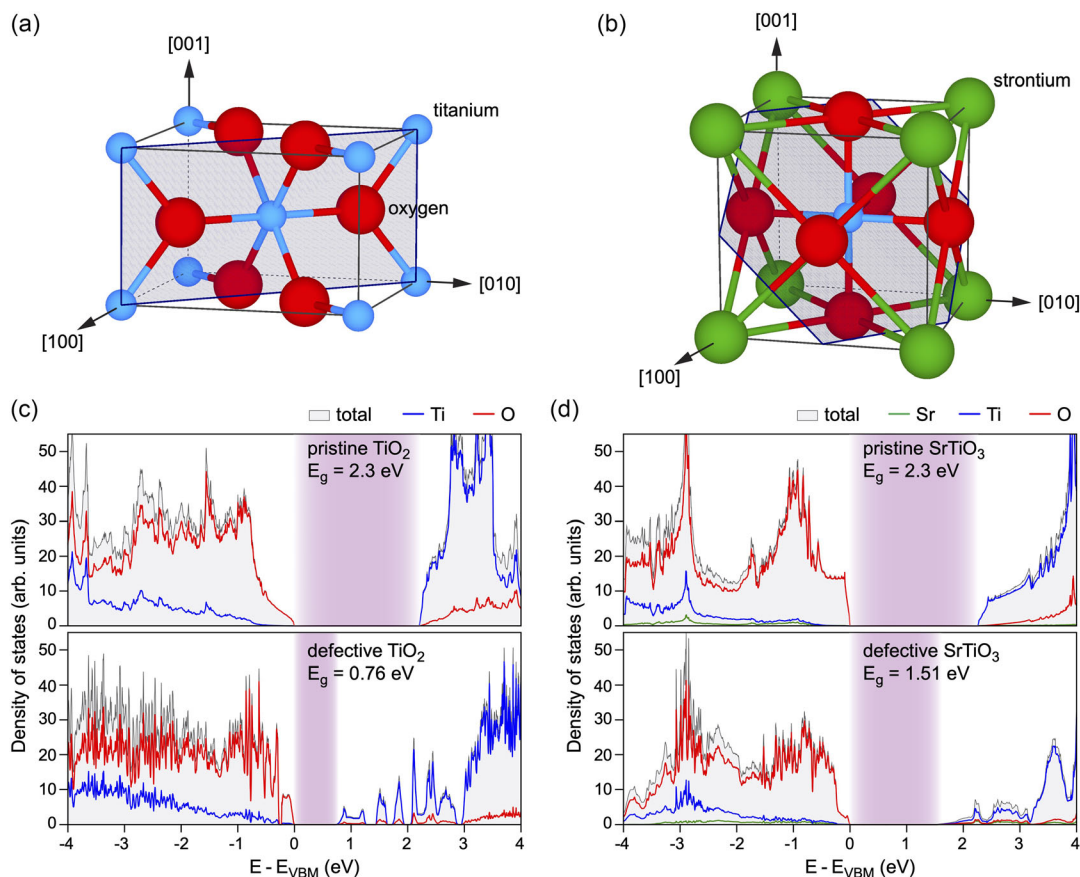


Figure 6. a) Bulk structures of rutile and b) strontium titanate. The TiO₂(110) and SrTiO₃(111) planes are shaded in (a) and (b), respectively. Color code used throughout this work: Sr—green spheres; Ti—blue spheres; O—red spheres. Density of states calculated for the pristine and defective c) bulk TiO₂ and d) bulk SrTiO₃ (see text for details).

In the next we discuss the surface terminations, which, judging by the experimental data presented above, form the interface. The rutile (110) surface (shaded area in Figure 6a) is the most stable crystal face. Along the [110]-direction TiO_2 consists of a mixed Ti–O layer, sandwiched between two layers of oxygen atoms (i.e., the $-\text{O}-(\text{T}-\text{O})-\text{O}-$ sequences, Figure 7a). The new lattice parameters are: $a_{\text{TiO}_2}^{110} = c_{\text{TiO}_2}^{\text{bulk}} = 3.03 \text{ \AA}$, $b_{\text{TiO}_2}^{110} = a_{\text{TiO}_2}^{\text{bulk}} \times \sqrt{2} = 6.62 \text{ \AA}$. $\text{SrTiO}_3(111)$ (shaded area in Figure 6b) is a polar surface. SrTiO_3 along the [111]-direction consists of alternating layers of SrO_3^{4-} and Ti^{4+} , which are each stacked in a “ABCABC...” manner (Figure 7b). The resulting unit cell has a hexagonal symmetry, but for convenience in this study we consider a tetragonal one, which has the following parameters: $a_{\text{SrTiO}_3}^{111} = a_{\text{SrTiO}_3}^{\text{bulk}} \times \sqrt{2} = 5.61 \text{ \AA}$, $b_{\text{SrTiO}_3}^{111} = a_{\text{SrTiO}_3}^{\text{bulk}} \times 2\sqrt{3}/2 = 9.72 \text{ \AA}$.

When modeling the interface, we considered two possibilities: 1) R0-structure, which has a $(2 \times 3)R0$ lateral periodicity with respect to the $\text{TiO}_2(110)$ unit cell marked in Figure 7a and $(1 \times 2)R0$ lateral periodicity with respect to the $\text{SrTiO}_3(110)$ unit cell marked in Figure 7b ($a_{\text{R0}}^{\text{init}} = 5.84 \text{ \AA}$ and $b_{\text{R0}}^{\text{init}} = 19.65 \text{ \AA}$); 2) R90-structure, which has a $(3 \times 2)R0$ lateral periodicity with respect to the $\text{TiO}_2(110)$ unit cell marked in Figure 7a and $(1 \times 2)R90$ lateral periodicity with respect to the $\text{SrTiO}_3(110)$ surface unit cell marked in Figure 7b ($a_{\text{R90}}^{\text{init}} = 9.41 \text{ \AA}$ and $b_{\text{R90}}^{\text{init}} = 12.23 \text{ \AA}$). In each case, the 3D structure under consideration consists

of nine SrO_3^{4-} sublayers and ten Ti^{4+} sublayers of $\text{SrTiO}_3(111)$, seven $-\text{O}-(\text{Ti}-\text{O})-\text{O}-$ layers of $\text{TiO}_2(110)$, and two additional O layers at the interfaces between the SrTiO_3 and TiO_2 stacks. These STO–TO compositions, consisting of 448 atoms each, were fully relaxed and the resulting structures (x, y, z -coordinates) can be found in the Supporting Information (Structure_R0.txt and Structure_R90.txt, Supporting Information). The difference in energy between them is only 43 meV atom^{-1} .

For the both structures under study, the calculated density of states (DOS) is similar to each other. Here, we present the DOS calculated for the R0-structure (Figure 8a), which is lower in energy, and the results for the R90-structure can be found in Figure S2, Supporting Information. Figure 8b shows DOS projected onto different layers as indicated in (a) subplot of this figure. While the levels away from the interface resemble the DOS of the respective bulk material, new states in DOS arise due to the interface layer, which have mostly TiO_x character (cf., Figure 6c,d). Still, the whole systems remain semiconducting with an unchanged bandgap. This means that the charge-carrier separation at the phase boundary will occur as follows without any loss in efficiency. Furthermore, the charge transfer between the phases yields arising dipole moment at the interface, which expected to promote the water splitting reaction.

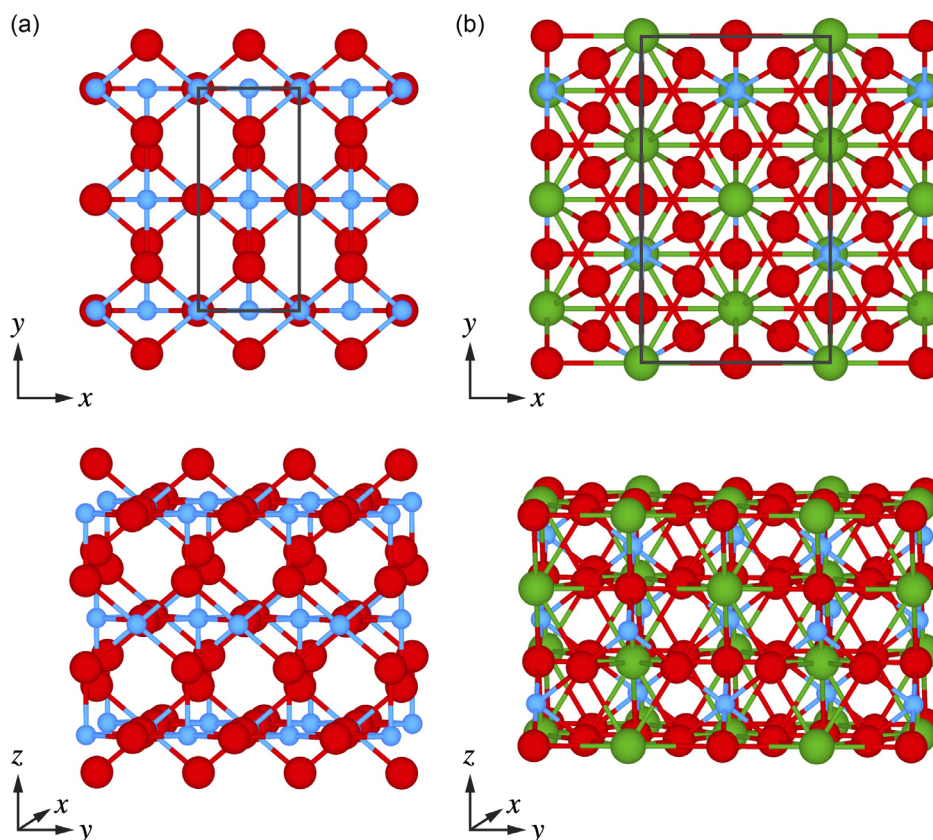


Figure 7. Top and side views of the a) bulk TiO_2 along the [110]-direction and b) bulk SrTiO_3 along the [111]-direction. The black rectangles indicate the unit cells considered in this work (see the text for details).

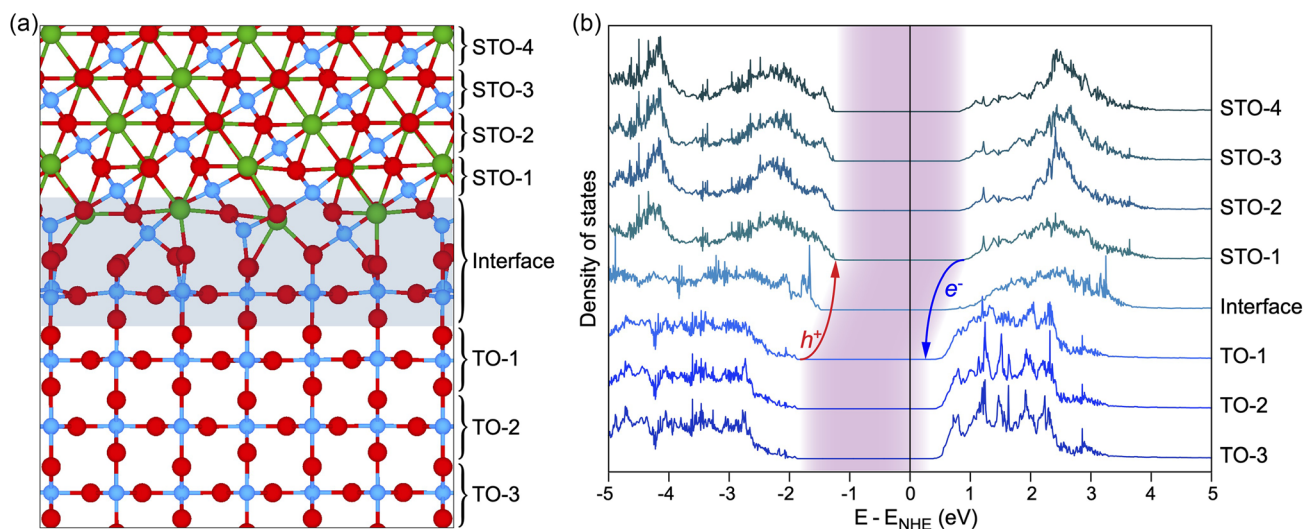


Figure 8. a) Side view of the relaxed R0-structure. Shaded area indicates the interface layer. b) Density of states projected onto different layers of the R0-structure as defined in (a). Energy is scaled with respect to the NHE level taken as zero. Shaded area indicates the bandgap. Blue and red arrows show the charge-carrier separation mechanism at the interface (see text for details).

The charge-carrier separation mechanism is schematically shown in Figure 8b: photoexcited electrons in the SrTiO₃ phase overcome the energetic barrier of TiO₂ (blue arrow in Figure 8b) and continue moving toward the cathode, while the holes generated in the TiO₂ phase overcome the energy barrier of SrTiO₃ band (red arrow in Figure 8b) and move toward the anode surface, where the process of water oxidation takes place. Hydrogen ions, the product of water splitting, are released into the electrolyte solution and reduced to gaseous hydrogen by the photo-generated electrons on the counter electrode's surface. Thus, the studied STO–TO system promotes charge-carrier separation and offers stability under conditions of extended photoelectrochemical water splitting.

3. Conclusion

In summary, using a combination of surface-sensitive (XPS, EDX/SEM) and bulk-sensitive (XRD, EDX/HR-TEM) experimental methods we have studied the effects of thermal annealing on the structural properties of SrTiO₃–TiO₂ eutectic compound. It is found that as-grown samples have a very diffuse interface between two semiconducting phases which is transformed to the sharp interface upon thermal annealing. The black color of the SrTiO₃–TiO₂ sample is defined by the large number of the noncompensated oxygen vacancies as confirmed by different experimental techniques. The crystallographic structure and electronic properties of this SrTiO₃–TiO₂ interface are found using HR-TEM and modeled using large-scale DFT calculations. It is found that the electronic structure of the joint eutectic compound is a sum of the respective contributions from both phases allowing the effective electron–hole separation at the SrTiO₃–TiO₂ interface. Our experimental and theoretical studies shed the light on the properties of this interesting class of materials and can be used for further improvements of their efficiency in water splitting reactions and in other application areas.

4. Experimental Section

Experiment: Samples in the present study were obtained from the bulk STO–TO eutectic rod (dia. ≈3 mm), which was synthesized using the μ -pulling method from the mixture of SrCO₃ and TiO₂ (rutile and anatase phases) powders with growth rate of 1 mm min⁻¹ according to the recipe published earlier in ref. [18]. STO–TO eutectic rod was cut into several slices with a thickness of ≈0.5–1 mm and then made one-side polished with a surface roughness below 100 nm. Before XPS analysis, the polished samples were ultrasonically cleaned using ethanol at 50 °C for 15 min. For XPS experiments, the STO–TO samples were mounted on Mo sample holders and then were stepwise annealed under UHV conditions; every annealing step is 60 min. Temperature of the sample was measured using calibrated pyrometer. Laboratory-based XPS experiments were performed in UHV station installed at Shanghai University and consisting of preparation and analysis chambers with a base pressure better than 1×10^{-10} mbar (SPECS Surface Nano Analysis GmbH). XPS spectra were measured using a monochromatized Al K α ($h\nu = 1486.6$ eV) X-ray source and SPECS PHOIBOS 150 hemispherical analyzer combined with a 2D-CMOS detector.

XRD patterns were collected at room temperature with a Desktop Bruker D2 Phaser diffractometer using Cu K α (1.54178 Å) radiation. SEM/EDX data were collected using ZEISS SIGMA 500 microscope. HR-TEM measurements were performed using an FEI Talos F200x G2 instrument combined with EDX (super-X) and the FIB preparation was performed using an FEI Scios 2 HiVac. UV–vis spectra were measured at room temperature using Shimadzu UV-3600i Plus UV–vis–NIR spectrophotometer.

Theory: The DFT calculations based on plane-wave basis sets of 400 eV cutoff energy were performed with the Vienna ab initio simulation package (VASP).^[32,33] The Perdew–Burke–Ernzerhof (PBE) exchange–correlation functional^[34] was employed. The electron–ion interaction was described within the projector augmented wave (PAW) method^[35] with Sr (4s, 4p, 5s), Ti (3d, 4s), and O (2s, 2p) states treated as valence states. The Brillouin-zone integration was performed on Γ -centered symmetry reduced Monkhorst–Pack meshes using a Gaussian smearing with $\sigma = 0.05$ eV, except for the calculation of total energies and DOSs. For those calculations, the tetrahedron method with Blöchl corrections^[36] was employed. $8 \times 8 \times 16$ and $16 \times 16 \times 16$ k -meshes were used for bulk TiO₂ and SrTiO₃, respectively, and they were proportionally modified when studying the supercells. The DFT + U scheme^[37,38] was adopted for the

treatment of Ti 3d orbitals, with the parameter $U_{\text{eff}} = U - J$ equal to 4 eV. For comparison reasons, selected calculations were performed using the HSE06 functional.^[39] The structures were fully relaxed until forces became smaller than 0.02 eV Å⁻¹.

Supporting Information

Supporting Information is available from the Wiley Online Library or from the author.

Acknowledgements

The authors thank the National Natural Science Foundation of China (grant no. 22272104) for financial support. E.V. gratefully acknowledges the computing time granted by the Resource Allocation Board and provided on the supercomputer Lise and Emmy at NHR@ZIB and NHR@Göttingen as part of the NHR infrastructure.

Conflict of Interest

The authors declare no conflict of interest.

Data Availability Statement

The data that support the findings of this study are available from the corresponding author upon reasonable request.

Keywords

electronic properties, eutectic, interface structures, SrTiO₃-TiO₂

Received: July 12, 2023

Revised: August 9, 2023

Published online: August 30, 2023

- [1] C. Jiang, S. J. A. Moniz, A. Wang, T. Zhang, J. Tang, *Chem. Soc. Rev.* **2017**, *46*, 4645.
- [2] R. D. Tentu, S. Basu, *Curr. Opin. Electrochem.* **2017**, *5*, 56.
- [3] H. M. Zeeshan, S. Sharma, M. Panahi, E. Voloshina, Y. Dedkov, *Phys. Chem. Chem. Phys.* **2022**, *24* 25720.
- [4] A. A. Ismail, D. W. Bahnemann, *Sol. Energy Mater. Sol. Cells* **2014**, *128* 85.
- [5] R. Li, *Chinese J. Catal.* **2017**, *38*, 5.
- [6] A. Fujishima, K. Honda, *Nature* **1972**, *238*, 37.
- [7] A. Fujishima, X. Zhang, D. A. Tryk, *Surf. Sci. Rep.* **2008**, *63*, 515.
- [8] Y. Sun, Z. Sun, S. Gao, H. Cheng, Q. Liu, F. Lei, S. Wei, Y. Xie, *Adv. Energy Mater.* **2014**, *4*, 1300611.
- [9] P. Zhang, J. Zhang, J. Gong, *Chem. Soc. Rev.* **2014**, *43*, 4395.

- [10] Y. Han, J. Wu, Y. Li, X. Gu, T. He, Y. Zhao, H. Huang, Y. Liu, Z. Kang, *Appl. Catal. B* **2022**, *304* 120983.
- [11] N. Li, X. Zou, M. Liu, L. Wei, Q. Shen, R. Bibi, C. Xu, Q. Ma, J. Zhou, *J. Phys. Chem. C* **2017**, *121*, 25795.
- [12] W. R. Duncan, O. V. Prezhdo, *Ann. Rev. Phys. Chem.* **2007**, *58*, 143.
- [13] H. Eidsvag, S. Bentouba, P. Vajeeston, S. Yohi, D. Velauthapillai, *Molecules* **2021**, *26*, 1687.
- [14] M. Niu, R. Cui, H. Wu, D. Cheng, D. Cao, *J. Phys. Chem. C* **2015**, *119*, 13425.
- [15] X. Chen, L. Liu, P. Y. Yu, S. S. Mao, *Science* **2011**, *331*, 746.
- [16] S. Chen, Y. Wang, J. Li, Z. Hu, H. Zhao, W. Xie, Z. Wei, *Mater. Res. Bull.* **2018**, *98* 280.
- [17] K. Bienkowski, S. Turczynski, R. Diduszko, M. Gajc, E. Gorecka, D. A. Pawlak, *Cryst. Growth Des.* **2011**, *11*, 3935.
- [18] K. Wysmulek, J. Sar, P. Osewski, K. Orliński, K. Kolodziejak, A. Trenzczek-Zajac, M. Radecka, D. A. Pawlak, *Appl. Catal. B* **2017**, *206* 538.
- [19] Y. Yokota, S. Horii, H. Ogino, M. Yoshino, A. Yamaji, Y. Ohashi, S. Kurosawa, K. Kamada, A. Yoshikawa, *J. Electron. Mater.* **2019**, *48*, 1827.
- [20] B. A. Pinaud, P. C. K. Vesborg, T. F. Jaramillo, *J. Phys. Chem. C* **2012**, *116*, 15918.
- [21] C. Cheng, R. Long, *J. Phys. Chem. Lett.* **2021**, *12*, 12040.
- [22] M. E. Zvanut, S. Jeddy, E. Towett, G. M. Janowski, C. Brooks, D. Schlom, *J. Appl. Phys.* **2008**, *104*, 064122.
- [23] F. Lei, Y. Sun, K. Liu, S. Gao, L. Liang, B. Pan, Y. Xie, *J. Am. Chem. Soc.* **2014**, *136*, 6826.
- [24] N. Zhang, D. Chen, F. Niu, S. Wang, L. Qin, Y. Huang, *Sci. Rep.* **2016**, *6*, 26467.
- [25] Y. Zhao, Y. Zhu, J. Zhu, H. Wang, Z. Ma, L. Gao, Y. Liu, K. Yang, Y. Shu, J. He, *J. Mater. Sci. Technol.* **2022**, *104* 172.
- [26] U. Diebold, *Surf. Sci. Rep.* **2003**, *48*, 53.
- [27] M. Rogala, G. Bihlmayer, P. Dabrowski, C. Rodenbücher, D. Wrana, F. Krok, Z. Klusek, K. Szot, *Sci. Rep.* **2019**, *9*, 12563.
- [28] S.-H. Zhang, J.-O. Wang, H.-J. Qian, R. Wu, N. Zhang, T. Lei, C. Liu, I. Kurash, *Chin. Phys. B* **2015**, *24*, 027901.
- [29] P. V. Nagarkar, P. C. Searson, F. D. Gealy, *J. Appl. Phys.* **1991**, *69*, 459.
- [30] K. Kolodziejak, J. Sar, K. Wysmulek, P. Osewski, M. Warczak, A. Sadkowski, M. Radecka, D. A. Pawlak, *J. Catal.* **2017**, *352* 93.
- [31] M. Schmidbauer, A. Kwasniewski, J. Schwarzkopf, *Acta Cryst.* **2012**, *68*, 8.
- [32] G. Kresse, J. Furthmüller, *Phys. Rev. B* **1996**, *54*, 11169.
- [33] G. Kresse, D. Joubert, *Phys. Rev. B* **1999**, *59*, 1758.
- [34] J. P. Perdew, K. Burke, M. Ernzerhof, *Phys. Rev. Lett.* **1996**, *77*, 3865.
- [35] P. E. Blöchl, *Phys. Rev. B* **1994**, *50*, 17953.
- [36] P. E. Blöchl, O. Jepsen, O. K. Andersen, *Phys. Rev. B* **1994**, *49*, 16223.
- [37] V. I. Anisimov, F. Aryasetiawan, A. I. Lichtenstein, *J. Phys. Condens. Matter* **1997**, *9*, 767.
- [38] S. L. Dudarev, G. A. Botton, S. Y. Savrasov, C. J. Humphreys, A. P. Sutton, *Phys. Rev. B* **1998**, *57*, 1505.
- [39] J. Heyd, G. E. Scuseria, M. Ernzerhof, *J. Chem. Phys.* **2003**, *118*, 8207.